Journal of Materials Chemistry A

ROYAL SOCIETY OF CHEMISTRY

PAPER

View Article Online
View Journal | View Issue

Cite this: J. Mater. Chem. A, 2021, 9, 19734

Photothermal effect enables markedly enhanced oxygen reduction and evolution activities for high-performance Zn–air batteries†

Xiaoyan Zhang, Shuang Pan, Huanhuan Song, Wengai Guo, Fan Gu, Chengzhan Yan, Huile Jin, Lijie Zhang, Yihuang Chen * and Shun Wang *

The ability to craft high-performance and cost-effective bifunctional oxygen catalysts opens up pivotal perspectives for commercialization of zinc–air batteries (ZABs). Despite recent grand advances in the development of synthetic techniques, the overall performance of electrocatalytic processes enters the bottleneck stage through focusing only on the design and modification of bifunctional catalyst materials. Herein, we report a simple yet robust strategy to markedly boost the performance of ZABs *via* capitalizing on the photothermal effect. Concretely, a bifunctional electrocatalyst comprising Co_3O_4 nanoparticles encapsulated within N-doped reduced graphene oxide (denoted as Co_3O_4/N-rGO) acted as both active material and photothermal component. Upon light illumination, the compelling photothermal effect of Co_3O_4/N-rGO rendered a localized and instant heating of the electrode with more active sites, enhanced electrical conductivity and improved release of bubbles. As such, a prominently reduced indicator ΔE of 0.635 V was realized, significantly outperforming recently reported systems (usually >0.68 V). Corresponding rechargeable ZABs based on Co_3O_4/N-rGO air electrodes possessed an excellent maximum power density of 299 mW cm^{-2} (1.8 times that of Pt/Ru-based ZABs) assisted by the photothermal effect with a superb cycling stability (over 500 cycles). This intensification strategy opens vast possibilities to ameliorate the performance of catalysts *via* innovatively and conveniently utilizing their photothermal feature, which may advance future application in high-performance ZABs and other energy conversion and storage systems.

Received 30th April 2021
Accepted 21st June 2021

DOI: 10.1039/d1ta03652a

rsc.li/materials-a

Introduction

The global demand for development of energy supply and storage systems is more urgent than ever.[1,2] Currently, lithium-ion batteries (LIBs) represent one advanced technique which has been widely used for rechargeable devices. However, their relatively low theoretical energy density and potential safety hazard adversely hinder the realization of a safe, green and economic future.[3,4] As a promising alternative to LIBs, rechargeable zinc–air batteries (ZABs) have garnered particular attention due to their cost-effectiveness, environmental friendliness, intrinsic nonflammability and high energy density.[5,6] Notwithstanding these impressive advantages, ZAB is still in its infancy. Concretely, the inherent sluggish kinetics of oxygen reduction and oxygen evolution reactions (ORR and OER) at the air cathode severely enlarges the charging/discharging voltage gaps[7–9] with low energy efficiencies.[10,11] While Pt and Ru/Ir-based electrocatalysts exhibit high ORR and OER activities, respectively, their instability, scarcity, exorbitant price as well as the lack of bifunctionality significantly limit their practical utilization in ZABs.[11–13] Clearly, it is highly desirable to craft low-cost, efficient and stable bifunctional electrocatalysts for commercialization of ZABs.

Among various nonprecious electrocatalysts, cobalt oxide (especially spinel-type Co_3O_4) nanomaterials have emerged as an efficient candidate owing to their natural abundance, eco-friendliness and low price.[14–16] Intriguingly, the structure of Co_3O_4 typically comprises multivalent elements (*i.e.*, Co^{2+}/Co^{3+}), which facilitates the electrocatalytic performance in principle.[14–19] The nanostructured design (*e.g.*, nanoparticle) of Co_3O_4 further increases the portion of surface active sites. Unfortunately, its practical competitiveness is seriously plagued by the inherently poor electrical conductivity. To tackle this issue, modification of Co_3O_4 with plentiful conductive materials has been adopted to improve the overall electrocatalytic activity.[20] For instance, heteroatom-doped (*i.e.*, N, S and B) graphene not only acts as a superb conductive substrate attributed to its outstanding electrical conductivity, but also promotes ORR/OER electrocatalysis owing to its unique surface electronic structure.[21,22] Meanwhile, the layered graphene with

College of Chemistry and Materials Engineering, Institute of New Materials and Industrial Technologies, Wenzhou University, Wenzhou 325035, PR China. E-mail: yhchen@wzu.edu.cn; shunwang@wzu.edu.cn

† Electronic supplementary information (ESI) available. See DOI: 10.1039/d1ta03652a

large specific surface area averts the aggregation of Co_3O_4 nanomaterials, leading to improved stability. However, despite recent impressive advances in Co_3O_4/graphene nanohybrids as bifunctional electrocatalysts,[23,24] their performance has gradually entered the bottleneck period *via* only the design and modification of catalysts. Obviously, the development of simple yet effective strategies to further improve the overall performance of Co_3O_4/graphene nanohybrids represents a pivotal endeavor towards the advancement of ZABs. This, however, has yet to be largely explored.

It is noteworthy that, recently, elevating operation temperature has shown the feasibility to further ameliorate the electrocatalytic process of Co-based electrodes.[25,26] For instance, the current density at 1.54 V *versus* reversible hydrogen electrode (RHE, V_{RHE}) of Co_3O_4 catalysts during the OER increased by 20 times when the temperature was raised from 25 to 65 °C.[26] The significant improvement *via* thermal energy can be ascribed to the following multiple factors based on Arrhenius' law. Upon heating, the effective collisions between reactant molecules are promoted with higher possibility to overcome the energy barrier during the reaction.[27,28] Furthermore, heating could facilitate the increased electrical conductivity and surface reconstruction of catalysts with boosted electrocatalytic kinetics.[29,30] However, traditional heating systems usually contain cumbersome equipment (*e.g.*, hot plate[31] and photovoltaic cell[26]) and inevitably heat up the electrolyte, resulting in reduced durability and security of electrocatalytic systems and unnecessary cost for extra energy input. In sharp contrast, photothermal effect provides a localized and efficient heating in a remote, instantaneous and economic way.[32,33] The construction of electrocatalysts with the photothermal effect (*i.e.*, photothermal electrocatalysts) enables *in situ* heating of the working electrode upon light illumination, thus avoiding the utilization of additional complex devices and energy wastage.[32,33] For instance, we recently achieved enhancement of the kinetics of water oxidation with the assistance of the photothermal effect.[34,35] Despite the recent copious work on nanomaterials containing Co_3O_4 and (or) graphene for photothermal therapy[36,37] and utilization of semiconductor-induced photogenerated charges,[38] their exploitation as photothermal-assisted bifunctional electrocatalysts in ZABs has rarely been reported.

Herein, we report the implementation of the photothermal effect within a robust bifunctional electrocatalyst composed of Co_3O_4 nanoparticles homogeneously dispersed in N-doped reduced graphene oxide (denoted as Co_3O_4/N-rGO) to dramatically boost the overall performance of ZABs. Specifically, Co_3O_4/N-rGO nanohybrids served as both active components and photothermal materials. Upon light irradiation, the ORR and OER properties of Co_3O_4/N-rGO were significantly enhanced, resulting in a remarkable ΔE (0.635 V) compared to that in the dark (0.694 V) and far exceeding that of the Pt/Ru-based benchmark catalyst and most reported earth-abundant systems (>0.68 V in general). The improved electrocatalytic performance can be attributed to the superior electrical conductivity, bubble evolution as well as enlarged active sites. Photothermal-assisted rechargeable ZABs with Co_3O_4/N-rGO as air electrodes exhibited outstanding cycling stability over 500 cycles and a superb maximum power density of 299 mW cm^{-2}, which was 1.7 times as much as that of the case without light illumination (175 mW cm^{-2}) and significantly surpassing the most reported systems. Overall, this work innovatively represents a convenient and robust strategy to accelerate the electrocatalytic reactivity *via* utilizing the photothermal effect, which opens an enticing avenue for the practical application of efficient ZABs and other catalytic processes.

Results and discussion

The formation of Co_3O_4/N-rGO was verified by transmission electron microscopy (TEM) and X-ray diffraction (XRD) with detailed morphological and structural information (Fig. 1). As shown in Fig. 1b–c and S1,† Co_3O_4 nanoparticles with an average diameter of 5 nm were evenly distributed on the surface of N-rGO. Conversely, the as-prepared pure GO without Co_3O_4 with a layer number of approximately 3–5 exhibited relatively low contrast (Fig. S2†). A representative high-resolution TEM (HRTEM) image (Fig. 1d) of Co_3O_4/N-rGO revealed their high crystallinity with lattice-fringe distances of 0.243, 0.202, and 0.285 nm, which matched well with the (311), (400), and (220) planes of spinel Co_3O_4, respectively. In addition, the corresponding selected area electron diffraction (SAED) pattern (Fig. S3†) also confirmed the spinel structure of Co_3O_4. The elemental mapping of Co_3O_4/N-rGO (Fig. 1e) clearly substantiated the uniform distribution of C, Co, O, and N across the entire substrate, further indicating the homogeneous N-doping and Co_3O_4 loading on the layered N-rGO. A typical XRD pattern of Co_3O_4/N-rGO is shown in Fig. 1f. The peaks at the 2θ scattering angles of 30.9°, 36.2°, 44.5°, 58.9° and 65.1° correlated with the diffractions from the (220), (311), (400), (511) and (440)

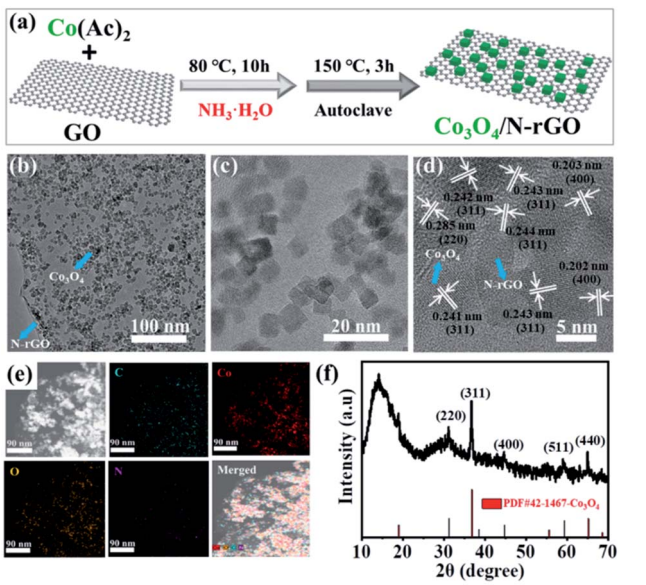

Fig. 1 (a) Synthetic strategy, (b, c) TEM with varied magnifications, (d) HRTEM, (e) elemental mapping images and (f) XRD pattern of CO_3O_4/N-rGO.

crystal planes of cubic Co_3O_4, respectively.[21] This result was consistent with the TEM measurements.

Fig. 2a shows the Raman investigation of Co_3O_4/N-rGO. The five distinct peaks in the range of 150–750 cm^{-1} can be assigned to the F^3_{2g}, E_g, F^2_{2g}, F^1_{2g}, and A_{1g} vibration modes of spinel Co_3O_4.[24,39] In addition, peaks at 1351 cm^{-1} and 1598 cm^{-1} were identified as D and G bands of N-rGO,[40] which further confirmed that the hybrid nanomaterials were composed of N-rGO and Co_3O_4. As shown in Fig. 2b, the intensity ratio of the D band to the G band (*i.e.*, I_D/I_G) of Co_3O_4/N-rGO increased in comparison with that of GO, revealing the successful reduction of GO to rGO.[41] By thermogravimetric analysis (TGA), the weight fraction of Co_3O_4 in hybrid nanomaterials was determined to be about 57.86 wt% (Fig. S4†). On the basis of the nitrogen adsorption–desorption (Fig. 2c and S5†), Co_3O_4/N-rGO catalyst possessed a high specific surface area of 116.02 $m^2\ g^{-1}$, pore volume of 0.142 $cm^3\ g^{-1}$, and average pore size of ~4.3 nm. The relatively high specific surface area of Co_3O_4/N-rGO facilitated the accessibility of active sites for electrocatalysis.

The chemical composition and bonding configuration were then scrutinized *via* X-ray photoelectron spectroscopy (XPS) measurements (Fig. 2d–f and S6†). As expected, a N 1s peak with a content of 3.49% was observed in the hybrid nanomaterials (Fig. 2d), demonstrating that N was successfully doped in the rGO.[42] The high-resolution N 1s spectrum (Fig. 2e) can further be fitted into three sub-peaks centered at 397.78 eV (pyridinic N), 398.91 eV (pyrrolic N), and 399.79 eV (graphitic N). It has been proved that pyridinic and graphitic N displayed outstanding electron-accepting ability to promote oxygen adsorption and thus decrease the overpotential of the ORR,[20] while pyridinic and pyrrolic N with lone-pair electrons can act as metal coordination sites.[42] The high-resolution spectrum of Co 2p in Fig. 2f exhibited two different types of Co species attributed to Co $2p_{3/2}$ (780.23 eV) and Co $2p_{1/2}$ (795.45 eV). When the Co 2p peaks were further deconvoluted to uncover the chemical state of Co element, the sub-peaks at 797.09 and 781.61 eV were ascribed to Co^{2+} species, while 780.14 and 795.02 eV were assigned to Co^{3+} species.[43]

The photothermal effect of Co_3O_4/N-rGO was then systematically investigated. As shown in Fig. 3a, Co_3O_4/N-rGO solution exhibited a wide light absorption range up to 850 nm, which enabled the potential heat generation triggered *via* near infrared (NIR) light irradiation. Inspired by this obvious absorption, NIR laser was irradiated on the Co_3O_4/N-rGO electrode (in the electrolyte solution), the temperature of which was detected using an IR thermal camera. The temperature of the Co_3O_4/N-rGO electrode increased quickly to 85.2 °C in 3 minutes, showing a better photothermal conversion efficiency compared to N-rGO, Co_3O_4 and Co_3O_4/rGO (Fig. 3b–c and S7–S11†). Due to the heat transfer between water and the Co_3O_4/N-rGO electrode, its temperature eventually remained at 86.0 °C. It is noteworthy that, during the irradiation process, the temperature of most of the electrolyte was almost unchanged with temperature of about 20 °C (Fig. 3b and c), indicating that the light-induced heat was localized on the surface of the Co_3O_4/N-rGO electrode. Therefore, there was no potential influence of temperature fluctuation of the electrolyte and the reference electrode on the OER and ORR activities of Co_3O_4/N-rGO, which facilitated the establishment of the relationship between the photothermal effect and the electrocatalytic properties of Co_3O_4/N-rGO.

To identify the photothermal effect on the electrocatalytic performance, the OER activity of Co_3O_4/N-rGO hybrid nanomaterials was first systematically studied. As shown in Fig. 4a, Co_3O_4/N-rGO exhibited better OER performance than Co_3O_4/rGO, N-rGO, Co_3O_4 and commercial RuO_2. The overpotential at the current density of 10 mA cm^{-2} (η_{10}) of Co_3O_4/N-rGO was 299 mV, while the η_{10} of Co_3O_4/rGO, Co_3O_4 and commercial

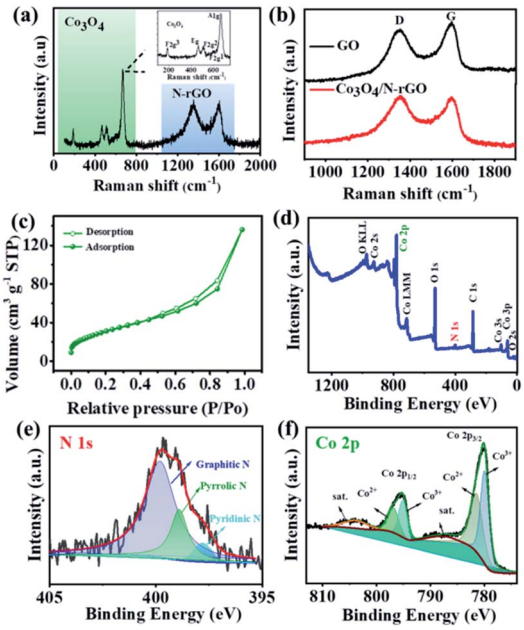

Fig. 2 (a) Raman spectra (inset: enlarged range of 150–750 cm^{-1}) of Co_3O_4/N-rGO. (b) Comparison of the Raman spectra of GO and Co_3O_4/N-rGO. (c) N_2 adsorption–desorption isotherm of Co_3O_4/N-rGO. XPS spectra of the (d) survey spectrum, (e) N 1s, and (f) Co 2p of the Co_3O_4/N-rGO.

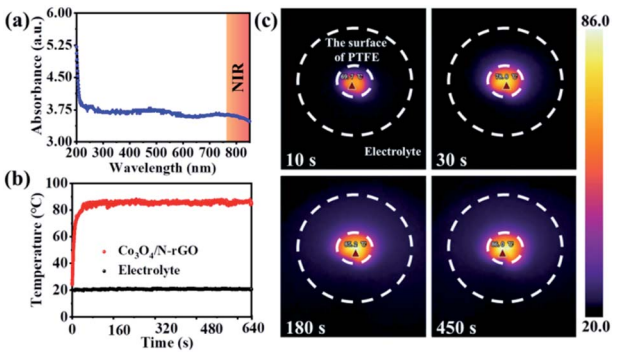

Fig. 3 (a) UV-Vis absorption spectrum and digital image of Co_3O_4/N-rGO. (b) Temperature variation over time of Co_3O_4/N-rGO and electrolyte solution under 808 nm NIR irradiation. (c) Corresponding infrared images of the electrode in the electrolyte at different times. The areas of polytetrafluoroethylene (PTFE) and catalyst are indicated by dashed outer and inner circles, respectively.

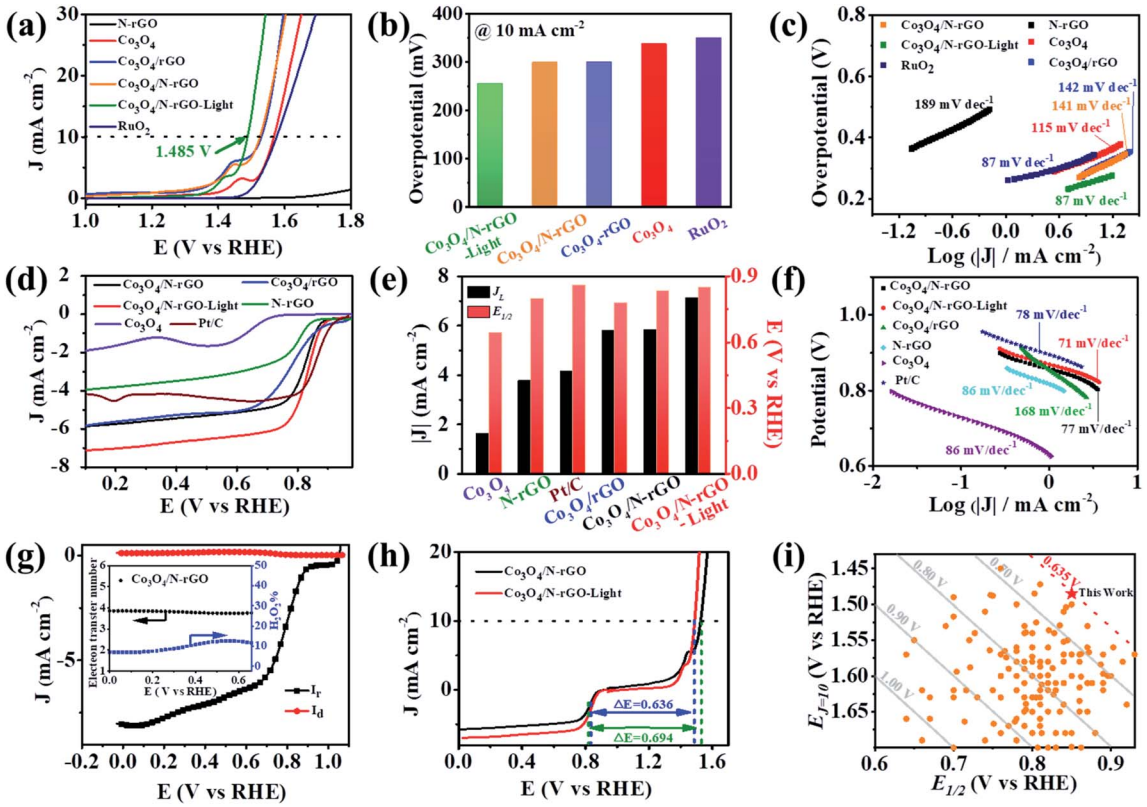

Fig. 4 (a) LSV, (b) corresponding overpotential at 10 mA cm^{-2}, and (c) Tafel curves of various electrodes for the OER in 1 M KOH. Co_3O_4/N-rGO-light represents the case of the Co_3O_4/N-rGO electrode under light illumination. (d) LSV curves, (e) corresponding $E_{1/2}$ and J_L, and (f) Tafel curves of various electrodes for the ORR in 0.1 M KOH. (g) RRDE measurements of the Co_3O_4/N-rGO electrode and the corresponding electron transfer number and the percentage of H_2O_2 at various potentials (inset). (h) Bifunctional catalytic curves of Co_3O_4/N-rGO with and without light. (i) The diagram for bifunctional performance comparison among Co_3O_4/N-rGO-light, and other reported bifunctional electrocatalysts (marked as the orange points).

RuO_2 was 300 mV, 337 mV and 350 mV, respectively, and N-rGO had no OER activity (Fig. 4b). Quite intriguingly, the photothermal effect further greatly enhanced the OER behavior of Co_3O_4/N-rGO as expected. Under NIR irradiation, the η_{10} of the Co_3O_4/N-rGO electrode reduced from 299 to 255 mV with a much smaller Tafel slope (from 141 to 87 mV/dec; Fig. 4c), reflecting the improved OER reaction kinetics of Co_3O_4/N-rGO *via* the photothermal effect. A similar observation was recorded in the cases of Co_3O_4/rGO, N-rGO and Co_3O_4 (Fig. S12†), suggesting the general yet simple strategy to enhance the OER performance *via* the photothermal effect. The response of the Co_3O_4/N-rGO electrode to the intermittent NIR light was very fast (Fig. S13†). Upon irradiation the current density increased significantly, which declined instantly once the light was off. These results indicated that the Co_3O_4/N-rGO electrode possessed marked photothermal conversion characteristics for improving the OER activity. In contrast, there was no photocurrent upon NIR light irradiation (Fig. S14†), which further verified that the increased current density of Co_3O_4/N-rGO was stimulated by the photothermal effect *via* NIR light irradiation.

To verify the bifunctional electrocatalytic activity of Co_3O_4/N-rGO, ORR performance was also investigated in 0.1 M KOH solution. A quasi-rectangular shaped CV with no significant reduction peak was observed in N_2-saturated KOH aqueous solution, while a characteristic reduction peak at 0.832 V appeared in the O_2-saturated electrolyte (Fig. S15a†), indicating the ORR electrocatalytic activity of Co_3O_4/N-rGO. Compared to pure Co_3O_4 or N-rGO, Co_3O_4/N-rGO exhibited higher ORR activity, resulting in a more positive onset potential (E_{onset} = 0.915 V), half-wave potential ($E_{1/2}$ = 0.835 V) and increased limiting current density (J_L = −5.76 mA cm^{-2}), as shown in Fig. 4d–f. It is noteworthy that the J_L and methanol tolerance (Fig. S15b†) of Co_3O_4/N-rGO were superior to those of Pt/C while the $E_{1/2}$ was only 0.029 V negative relative to Pt/C, reflecting the excellent ORR catalytic activity of Co_3O_4/N-rGO. To illustrate the ORR kinetics, the Koutecky–Levich analysis was conducted (Fig. S16–S17†). The calculated number of electrons transferred for Co_3O_4/N-rGO was close to 4.0 (Fig. S16b†), which was consistent with the value of about 3.9 obtained from the rotating ring disk electrode (RRDE) measurement (Fig. 4g). Moreover, the yield of H_2O_2 was less than 15% (Fig. 4g). All the above results indicated that the ORR of the Co_3O_4/N-rGO electrode followed a four-electron transfer process. Similarly, when exposed to 808 nm light, the E_{onset}, $E_{1/2}$ and J_L of Co_3O_4/N-rGO increased to 0.934 V, 0.850 V and −7.00 mA cm^{-2} (Fig. 4d, e), respectively, indicating that the ORR performance can also be significantly boosted *via* the photothermal effect. It was further confirmed by the lowest Tafel slope of Co_3O_4/N-rGO (71 mV

dec^{-1}) under NIR light irradiation, which was comparable with that of Pt/C (78 mV dec^{-1}), as shown in Fig. 4f. This photothermal conversion for boosting the ORR performance was convenient and general (Fig. S18–S19†).

The reversible oxygen electrode activity was then assessed *via* the potential difference ΔE between $E_{j=10}$ (potential at 10 mA cm^{-2}) in the OER and $E_{1/2}$ in the ORR (*i.e.*, $\Delta E = E_{j=10} - E_{1/2}$). A lower ΔE value generally indicates a better bifunctional activity.[44] As shown in Fig. 4h, S20 and Table S1,† the ΔE value of the Co_3O_4/N-rGO bifunctional electrocatalyst was 0.694 V and further decreased to 0.635 V under NIR irradiation. To intuitively verify the obtained excellent bifunctionality, Fig. 4i (corresponding detailed information in Tables S2–S4†) summarizes the recently reported bifunctional electrocatalysts. Clearly, most reported systems delivered ΔE values in the range of 0.68–0.90 V, substantiating the markedly improved bifunctionality enabled by the photothermal effect and therefore guaranteeing enhancement of the ZAB performance. In addition to the bifunctional activity, the durability of the electrode represented another important factor. As depicted in Fig. S21a and b,† Co_3O_4/N-rGO retained 86% (91%) of its initial OER activity with (without) light after 10 h, while there was only 22% retention in the case of commercial RuO_2. For the ORR, Co_3O_4/N-rGO also exhibited superior stability with (87.5% retention) and without (86% retention) light for 10 h compared with Pt/C (84% retention; Fig. S21c and d†). The excellent ORR and OER properties of Co_3O_4/N-rGO may be ascribed to multiple factors. First, the *in situ* growth of Co_3O_4 in N-rGO led to the close contact between the ultra-thin N-rGO and Co_3O_4 with improved overall conductivity, which was conducive to the electron transfer in the ORR and OER processes.[39] Second, the synergistic coupling of N-rGO and Co_3O_4 nanoparticles modified the electronic structure and promoted the adsorption/desorption steps of oxygen-containing reactants, thus enhancing the electrocatalytic process.[45] Third, the relatively high specific surface area of Co_3O_4 nanoparticles was maintained *via* the separation of N-rGO layers, therefore facilitating superb accessibility of active sites within the electrode.

The underlying mechanism of the photothermal effect of Co_3O_4/N-rGO catalysts on their electrocatalytic performance was then investigated. To this end, it is necessary to study the origin of the photothermal characteristic of Co_3O_4/N-rGO, which can be rationalized as follows. It is reported that the two-dimensional nanomaterials (*e.g.*, N-rGO) possess plasmonic effects with NIR light irradiation, thus promoting the light-to-heat conversion.[37] On the other hand, the photothermal effect of semiconductors (*e.g.*, Co_3O_4) is related to structural defects (*e.g.*, oxygen vacancies).[46] As shown in the O 1s XPS spectrum of Co_3O_4/N-rGO (Fig. S6†), a peak located at 531.2 eV was observed after deconvolution, verifying the presence of oxygen vacancies.[47] Besides, the peak at approximately 826 nm in the photoluminescence spectrum of Co_3O_4/N-rGO (Fig. S22†) was ascribed to the electron trap on the tetrahedral site related to oxygen vacancies.[48] Therefore, upon NIR light illumination, the excited electrons of Co_3O_4 nonradiatively recombine with holes through oxygen vacancy bridges, generating thermal radiation toward the surrounding environment *via* frequent vibration of the crystal lattice and leading to the photothermal characteristic of Co_3O_4.[46] A similar mechanism was reported to depict the photothermal effect of Fe_3O_4.[49] The synergistic effect and close contact between each component within Co_3O_4/N-rGO enabled improved photothermal conversion (Fig. 3 and S7–S10†). To gain insight into the photothermal effect on active sites in the electrode, the electrochemically active surface areas (ECSAs) were indicated *via* electrochemical double layer capacitance (C_{dl}).[50] As shown in Fig. S23,† Co_3O_4/N-rGO with NIR irradiation possessed a higher C_{dl} of 35 mF cm^{-2} than the same electrode without NIR irradiation (27 mF cm^{-2}). The increase in ECSA suggested that more accessible active sites were formed with the assistance of the photothermal effect. The increased temperature of the Co_3O_4/N-rGO electrode enabled by light was conducive to the infiltration of the electrolyte into the electrode materials, leading to more contact between the active sites and electrolyte, and thus a larger ECSA. The electrochemical impedance spectroscopy (EIS) Nyquist plots of the Co_3O_4/N-rGO electrode with and without light irradiation are depicted in Fig. S24.† The charge-transfer resistance (R_{ct}) at the high frequency range of the Nyquist plot was strongly associated with the electrocatalytic (*e.g.*, ORR) processes. Quite intriguingly, light irradiation reduced the R_{ct} of the Co_3O_4/N-rGO electrode due to the superior electron transfer at a light-triggered high temperature.[51] These EIS results further demonstrated the positive role of the photothermal effect on the carrier transport in the electrocatalytic process. Furthermore, the photothermal effect also showed the feasibility to improve the removal speed of small oxygen bubbles during the OER (Fig. S25–S26, Movie S1†). Additionally, the effective collisions between reactant molecules and the dissolved oxygen diffusion toward the electrode are promoted *via* photothermal heating, which helped overcome the activation barrier of the reaction and facilitated the ORR process, respectively.[27,28] On the basis of the above analysis, the enhanced electrocatalytic performance of Co_3O_4/N-rGO upon light illumination mainly originated from the boosted reaction dynamics, larger number of active sites, improved electron transfer, and easier release of bubbles.

Inspired by the outstanding bifunctional activity and stability of the as-prepared Co_3O_4/N-rGO electrocatalyst, a Zn–air battery (ZAB) was constructed with Co_3O_4/N-rGO and Zn foil as the air cathode and anode, respectively (Fig. 5a). The open-circuit voltage (OVC) of the Co_3O_4/N-rGO-based ZAB was about 1.459 V (Fig. 5b), which was higher than the OVC (1.426 V) of the ZAB based on Pt/C and RuO_2 (*i.e.*, Pt/Ru-based ZAB). It was able to power a commercial blue light-emitting diode (LED, 2.5 V) by using two series-connected Co_3O_4/N-rGO-based ZABs with an OVC of 2.826 V (Fig. S27†). In addition, the Co_3O_4/N-rGO-based ZAB displayed smaller charging voltages as well as charging/discharging voltage gaps than the Pt/Ru-based ZAB over the entire range of current density (Fig. 5c). As shown in Fig. 5d, the discharging voltages for the Co_3O_4/N-rGO-based ZAB were constantly higher than those of Pt/Ru-based ZAB, along with a superior maximum power density of 175.97 mW cm^{-2} (at ~282.5 mA cm^{-2}) for the former over that (166.50 mW cm^{-2}) of the latter.

Motivated by the superb performance of the Co_3O_4/N-rGO-based ZAB, its promotion induced by the photothermal effect

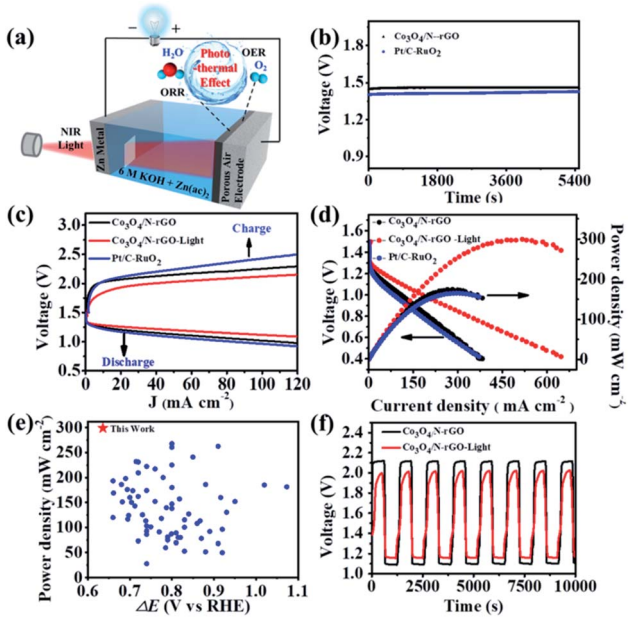

Fig. 5 (a) Scheme of the photothermal-assisted ZAB. (b) Open-circuit voltage plots of ZABs based on Co_3O_4/N-rGO and Pt/C + RuO_2 (mass ratio: 1 : 1) as air cathodes, respectively. (c) Charging/discharging polarization curves, (d) polarization and power density curves of ZABs based on Co_3O_4/N-rGO with and without light, and Pt/C + RuO_2. (e) The diagram for bifunctional performance comparison among the photothermal-assisted Co_3O_4/N-rGO-based ZAB, and other reported cathodes (marked as the blue points). (f) Cycling test of Co_3O_4/N-rGO-based ZABs with and without light.

was then scrutinized. The charging/discharging voltages were significantly improved with further reduced gaps under light (Fig. 5c), which matched well with the OER/ORR behaviors (Fig. 4). More importantly, the maximum power density was enhanced to 299.02 mW cm^{-2} in the presence of light (Fig. 5d), outperforming those of current advanced ZABs (Fig. 5e and corresponding detailed information in Tables S2–S4†). The specific capacity of the Co_3O_4/N-rGO-based ZAB with (or without) NIR irradiation reached 763 (or 723) mA h g^{-1}, which was comparable to that of the Pt/Ru-based ZAB (757 mA h g^{-1}) as shown in Fig. S28.† In addition, the discharging rate performance (Fig. S29†) was evaluated through recording the discharging voltages under varied current densities. As expected, the light illumination rendered the Co_3O_4/N-rGO-based ZAB with improved output voltages from 1.327, 1.315, 1.293, 1.269 and 1.232 V to 1.348, 1.336, 1.318, 1.299 and 1.272 V at current densities of 1, 2, 5, 10 and 20 mA cm^{-2}, respectively, while those for the Pt/Ru-based ZAB were only 1.311, 1.294, 1.268, 1.243 and 1.211 V. It is noteworthy that the discharging voltage of the Co_3O_4/N-rGO-based ZAB with (without) light rebounded to 1.315 (1.298) V when the current density returned from 20 to 5 mA cm^{-2}, indicating the excellent stability of the Co_3O_4/N-rGO cathode. The cycling stability of the rechargeable battery based on Co_3O_4/N-rGO was investigated at a current density of 10 mA cm^{-2} (Fig. 5f and S30†). After 500 discharging/charging cycles, the voltage gap difference of the Co_3O_4/N-rGO-based ZAB was negligible, indicating its excellent durability with Co_3O_4/N-rGO acting as a highly efficient and stable air electrode. Conversely, there was a substantial increase in the voltage gap (from 1.19 to 1.74 V) with a significant round-trip efficiency (RTE) drop (from 47% to 34%) for the Pt/Ru-based ZAB. Furthermore, the light irradiation triggered a reduced charging voltage from 2.11 to 1.98 V with an enhanced discharging voltage from 1.10 to 1.16 V (Fig. 5f), resulting in an obvious decrease in voltage gap from 1.02 to 0.82 V and a notable increase in RTE from ~52% to ~59%. Thus, our Co_3O_4/N-rGO-based ZAB manifests outstanding performance and stability assisted by the photothermal effect (Tables S3–S4†).

Conclusions

In conclusion, we developed a convenient and robust strategy for engineering high-performance ZABs *via* rationally and innovatively capitalizing on the compelling photothermal effect of the ORR/OER bifunctional catalyst. In sharp contrast to traditional heating strategies, the implementation of the photothermal effect enabled efficient and localized heating with significantly less energy input and improved convenience. Upon light irradiation, the electrocatalytic activities of both OER and ORR processes of Co_3O_4/N-rGO were greatly boosted simultaneously due to the enhanced electrical conductivity, bubble evolution as well as increased active sites. Specifically, only an η_{10} in the OER of 255 (299) mV and an $E_{1/2}$ in the ORR of 0.850 (0.835) V were required with a superb ΔE value of 0.635 (0.694) V in the presence (absence) of light, surpassing most of the state-of-the-art bifunctional electrocatalysts. Rechargeable ZABs based on the photothermal Co_3O_4/N-rGO cathode exhibited preeminent performance. Long-term stability with an extraordinary maximum power density of 299 mW cm^{-2} assisted by the photothermal effect was realized, which was 1.8 times as much as that of Pt/Ru-based ZABs. Our study provides a powerful platform to further enhance the performance of ZABs through innovatively utilizing the photothermal characteristic, which may underpin future developments of advanced catalytic materials and devices.

Conflicts of interest

There are no conflicts to declare.

Acknowledgements

The authors are thankful for the financial support from the National Natural Science Foundation of China (52072273, 51772219, 51872209), Zhejiang Provincial Natural Science Foundation of China (LQ21B030002), and Basic Science and Technology Research Project of Wenzhou (G2020007).

Notes and references

1 E. Pomerantseva, F. Bonaccorso, X. Feng, Y. Cui and Y. Gogotsi, *Science*, 2019, 366.
2 S. Pan, J. Li, Z. Wen, R. Lu, Q. Zhang, H. Jin, L. Zhang, Y. Chen and S. Wang, *Adv. Energy Mater.*, 2021, 2004002.

3 E. Fan, L. Li, Z. Wang, J. Lin, Y. Huang, Y. Yao, R. Chen and F. Wu, *Chem. Rev.*, 2020, **120**, 7020–7063.
4 S. Zhao, C. D. Sewell, R. Liu, S. Jia, Z. Wang, Y. He, K. Yuan, H. Jin, S. Wang, X. Liu and Z. Lin, *Adv. Energy Mater.*, 2019, **10**, 1902657.
5 M. Luo, W. Sun, B. B. Xu, H. Pan and Y. Jiang, *Adv. Energy Mater.*, 2020, **11**, 2002762.
6 J. Wu, B. Liu, X. Fan, J. Ding, X. Han, Y. Deng, W. Hu and C. Zhong, *Carbon Energy*, 2020, **2**, 370–386.
7 Y. Li and H. Dai, *Chem. Soc. Rev.*, 2014, **43**, 5257–5275.
8 D. Ren, J. Ying, M. Xiao, Y. P. Deng, J. Ou, J. Zhu, G. Liu, Y. Pei, S. Li, A. M. Jauhar, H. Jin, S. Wang, D. Su, A. Yu and Z. Chen, *Adv. Funct. Mater.*, 2019, **30**, 1908167.
9 X. Wang, Z. Zhu, L. Chai, J. Ding, L. Zhong, A. Dong, T.-T. Li, Y. Hu, J. Qian and S. Huang, *J. Power Sources*, 2019, **440**, 227158.
10 J. Zhu, M. Xiao, G. Li, S. Li, J. Zhang, G. Liu, L. Ma, T. Wu, J. Lu, A. Yu, D. Su, H. Jin, S. Wang and Z. Chen, *Adv. Energy Mater.*, 2019, **10**, 1903003.
11 P. Tan, B. Chen, H. Xu, H. Zhang, W. Cai, M. Ni, M. Liu and Z. Shao, *Energy Environ. Sci.*, 2017, **10**, 2056–2080.
12 M. Xiao, J. Zhu, G. Li, N. Li, S. Li, Z. P. Cano, L. Ma, P. Cui, P. Xu and G. Jiang, *Angew. Chem.*, 2019, **131**, 9742–9747.
13 C. Yang, H. Jin, C. Cui, J. Li, J. Wang, K. Amine, J. Lu and S. Wang, *Nano Energy*, 2018, **54**, 192–199.
14 Q. Wang, H. Miao, S. Sun, Y. Xue and Z. Liu, *Chemistry*, 2018, **24**, 14816–14823.
15 R. Zhang, Y.-C. Zhang, L. Pan, G.-Q. Shen, N. Mahmood, Y.-H. Ma, Y. Shi, W. Jia, L. Wang, X. Zhang, W. Xu and J.-J. Zou, *ACS Catal.*, 2018, **8**, 3803–3811.
16 T. Y. Ma, S. Dai, M. Jaroniec and S. Z. Qiao, *J. Am. Chem. Soc.*, 2014, **136**, 13925–13931.
17 Q. Zhao, Z. Yan, C. Chen and J. Chen, *Chem. Rev.*, 2017, **117**, 10121–10211.
18 C. P. Plaisance and R. A. van Santen, *J. Am. Chem. Soc.*, 2015, **137**, 14660–14672.
19 J. Xu, P. Gao and T. S. Zhao, *Energy Environ. Sci.*, 2012, **5**, 5333–5339.
20 G. Li, X. Wang, J. Fu, J. Li, M. G. Park, Y. Zhang, G. Lui and Z. Chen, *Angew. Chem., Int. Ed.*, 2016, **55**, 4977–4982.
21 Y. Liang, Y. Li, H. Wang, J. Zhou, J. Wang, T. Regier and H. Dai, *Nat. Mater.*, 2011, **10**, 780–786.
22 H. Jin, H. Huang, Y. He, X. Feng, S. Wang, L. Dai and J. Wang, *J. Am. Chem. Soc.*, 2015, **137**, 7588–7591.
23 K. Kumar, C. Canaff, J. Rousseau, S. Arrii-Clacens, T. W. Napporn, A. Habrioux and K. B. Kokoh, *J. Phys. Chem. C*, 2016, **120**, 7949–7958.
24 Y. Li, C. Zhong, J. Liu, X. Zeng, S. Qu, X. Han, Y. Deng, W. Hu and J. Lu, *Adv. Mater.*, 2018, **30**, 1703657.
25 J. Wang, L. Zhu, G. Dharan and G. W. Ho, *J. Mater. Chem. A*, 2017, **5**, 16580–16584.
26 G. Zhang, H. Wang, J. Yang, Q. Zhao, L. Yang, H. Tang, C. Liu, H. Chen, Y. Lin and F. Pan, *Inorg. Chem.*, 2018, **57**, 2766–2772.
27 B. Han and Y. H. Hu, *J. Phys. Chem. C*, 2015, **119**, 18927–18934.
28 M. W. Menzinger and R. Wolfgang, *Angew. Chem., Int. Ed.*, 1969, **8**, 438–444.
29 L. Gao, X. Cui, Z. Wang, C. D. Sewell, Z. Li, S. Liang, M. Zhang, J. Li, Y. Hu and Z. Lin, *Proc. Natl. Acad. Sci. U. S. A.*, 2021, **118**, e2023421118.
30 X. Liu, R. Guo, K. Ni, F. Xia, C. Niu, B. Wen, J. Meng, P. Wu, J. Wu, X. Wu and L. Mai, *Adv. Mater.*, 2020, **32**, e2001136.
31 L. Zhang, X. Ye, M. Boloor, A. Poletayev, N. A. Melosh and W. C. Chueh, *Energy Environ. Sci.*, 2016, **9**, 2044–2052.
32 L. Gu, C. Zhang, Y. Guo, J. Gao, Y. Yu and B. Zhang, *ACS Sustainable Chem. Eng.*, 2019, **7**, 3710–3714.
33 Y. Wu, S. Han, Y. Huang, Y. Shi and B. Zhang, *J. Mater. Chem. A*, 2018, **6**, 18426–18429.
34 M. Zhao, T. Chen, B. He, X. Hu, J. Huang, P. Yi, Y. Wang, Y. Chen, Z. Li and X. Liu, *J. Mater. Chem. A*, 2020, **8**, 15976–15983.
35 X. Hu, J. Huang, F. Zhao, P. Yi, B. He, Y. Wang, T. Chen, Y. Chen, Z. Li and X. Liu, *J. Mater. Chem. A*, 2020, **8**, 14915–14920.
36 M. Gao, L. Zhu, C. K. Peh and G. W. Ho, *Energy Environ. Sci.*, 2019, **12**, 841–864.
37 S. Liu, X. Pan and H. Liu, *Angew. Chem., Int. Ed.*, 2020, **59**, 5890–5900.
38 C. Tomon, S. Sarawutanukul, S. Duangdangchote, A. Krittayavathananon and M. Sawangphruk, *Chem. Commun.*, 2019, **55**, 5855–5858.
39 Z. Jiang, Z.-J. Jiang, T. Maiyalagan and A. Manthiram, *J. Mater. Chem. A*, 2016, **4**, 5877–5889.
40 Z. Wang, B. Li, X. Ge, F. W. Goh, X. Zhang, G. Du, D. Wuu, Z. Liu, T. S. Andy Hor, H. Zhang and Y. Zong, *Small*, 2016, **12**, 2580–2587.
41 L. Liu, Z. Niu, L. Zhang, W. Zhou, X. Chen and S. Xie, *Adv. Mater.*, 2014, **26**, 4855–4862.
42 X. Zhang, R. Liu, Y. Zang, G. Liu, G. Wang, Y. Zhang, H. Zhang and H. Zhao, *Chem. Commun.*, 2016, **52**, 5946–5949.
43 L. Xu, Q. Jiang, Z. Xiao, X. Li, J. Huo, S. Wang and L. Dai, *Angew. Chem., Int. Ed.*, 2016, **55**, 5277–5781.
44 J. Fu, F. M. Hassan, J. Li, D. U. Lee, A. R. Ghannoum, G. Lui, M. A. Hoque and Z. Chen, *Adv. Mater.*, 2016, **28**, 6421–6428.
45 M. Zeng, Y. Liu, F. Zhao, K. Nie, N. Han, X. Wang, W. Huang, X. Song, J. Zhong and Y. Li, *Adv. Funct. Mater.*, 2016, **26**, 4397–4404.
46 Y. Cheng, Y. Chang, Y. Feng, H. Jian, Z. Tang and H. Zhang, *Angew. Chem., Int. Ed.*, 2018, **57**, 246–251.
47 S. Wang, P. Chen, Y. Bai, J. H. Yun, G. Liu and L. Wang, *Adv. Mater.*, 2018, **30**, e1800486.
48 C. Mercado, Z. Seeley, A. Bandyopadhyay, S. Bose and J. L. McHale, *ACS Appl. Mater. Interfaces*, 2011, **3**, 2281–2288.
49 M. E. Sadat, M. Kaveh Baghbador, A. W. Dunn, H. P. Wagner, R. C. Ewing, J. Zhang, H. Xu, G. M. Pauletti, D. B. Mast and D. Shi, *Appl. Phys. Lett.*, 2014, **105**, 091903.
50 X. Zhang, J. Li, Y. Yang, S. Zhang, H. Zhu, X. Zhu, H. Xing, Y. Zhang, B. Huang, S. Guo and E. Wang, *Adv. Mater.*, 2018, **30**, e1803551.
51 P. Dias, T. Lopes, L. Meda, L. Andrade and A. Mendes, *Phys. Chem. Chem. Phys.*, 2016, **18**, 5232–5243.

